Numerical study on the behaviour of horizontal anchor using upgraded SANISAND-MS

Hongjian Lan [a], Hongfen Zhao [a,b,c,**], Haoyuan Liu [d,*]

[a] School of Civil Engineering, Sun Yat-sen University, Zhuhai, 519082, China
[b] State Key Laboratory for Tunnel Engineering, Guangzhou, 510275, China
[c] Guangdong Key Laboratory of Marine Civil Engineering, School of Civil Engineering, Sun Yat-sen University, Guangzhou, 510275, China
[d] Advanced Geomodelling Section, Norwegian Geotechnical Institute, Norway

ARTICLE INFO

ABSTRACT

Horizontal plate anchors are widely used to secure tension leg platforms via mooring lines. A thorough understanding of the monotonic, cyclic and post-cyclic behaviour of plate anchors is essential to accurately estimate plate anchors' capacity. This paper presents a systematic investigation of horizontal rectangular plate anchors subjected to vertical monotonic and cyclic loads in quartz sand under drained conditions using three-dimensional finite-element simulations. The upgraded SANISAND-MS model is employed to accurately capture sand's ratcheting behaviour. The monotonic uplift load is affected by the contact types used between the soil-anchor interface, and it increases with increasing embedded depth ratio, aspect ratio, and relative density. The results of cyclic tests reveal that in loose and dense sands, the cyclic amplitude ratio and cyclic asymmetric ratio affect the displacement accumulation at the cyclic stage. The cyclic loading leads to a higher post-cyclic uplift load than the monotonic tests. Moreover, the post-cyclic uplift load increases more in tests with a high cyclic amplitude ratio. Investigation on local soil responses shows that this can be attributed to sand's densification, which increases sand's strength and stiffness. The study also supports the development of long term analysis for anchoring systems subjected to cyclic loading in offshore applications.

1. Introduction

Plate anchors have been successfully used for oil and gas applications (Rigzone, 2006) and are being increasingly considered for mooring offshore floating renewable energy devices (Fontana et al., 2016; Hallowell et al., 2018). Anchor-type foundations provide resistance against uplift or lateral loading. The pullout behaviour of horizontal plate anchors under monotonic loads has been extensively studied. However, limited studies have been conducted on the cyclic behaviours of plate anchors subjected to long-term cyclic loading. The cyclic loading may affect the uplift capacity of the anchors, consequently affecting the mooring performance and overall system safety. Therefore, it is crucial to have a thorough understanding of the monotonic, cyclic and post-cyclic behaviour of plate anchors under long-term cyclic loading.

Studies of plate anchors in various types of soil have been widely reported in the literature. Most of the studies were conducted to evaluate the behaviour of plate anchors in soft clay, which is commonly encountered in very deep water environments. These studies are particularly relevant for oil and gas platforms operating in a water depth exceeding 800 m (Huang et al., 2020). Floating OWTs are typically located in relatively shallow water depths (e.g. < 100 m), where sandy seabed deposits are more common (Chow et al., 2015, 2018; Roy et al., 2021).

Plate anchors behave differently depending on their positioning and loading conditions. For example, horizontally embedded plate anchors are employed to anchor tension leg platforms (TLPs). The horizontally embedded anchors are subjected to vertical loads from the buoyancy of platforms as well as long-term cyclic loads induced by environmental waves and currents (Chow et al., 2015; Cheng et al., 2021). So far, the investigations into the behaviour of horizontally oriented plate anchors have primarily focused on estimating the ultimate uplift capacity under monotonic loading conditions. These studies have explored various factors such as embedded depths, soil densities and anchor shapes, and have identified different failure mechanisms, often with the aid of the

---

critical embedded depth (Merifield et al., 2006; Merifield and Sloan, 2006; Li et al., 2016; Zhang et al., 2017; Choudhary et al., 2018; Roy et al., 2021). However, the cyclic response of plate anchors in sands is a complex interaction problem and being less studied. During cyclic loading, sands can gradually accumulate plastic strains, which is known as ratcheting behaviour (Houlsby et al., 2017; Liu et al., 2019). Consequently, plate anchors embedded in sand may accumulate displacement over their full operating life and change the monotonic post-cycling capacity (Moghaddas Tafreshi et al., 2019). According to the experimental results reported by Chow et al. (2015, 2018, 2020), the static pullout capacity after cyclic loading could have a higher soil resistance under the drained condition. However, the mechanisms behind such performance still need further investigation.

Several approaches have been adopted to study the performance of plate anchors, including theoretical analysis (Rowe and Davis, 1982; White et al., 2008), physical testing (O'Loughlin and Barron, 2012; Chow et al., 2015; Moghaddas Tafreshi et al., 2019; Roy et al., 2021), macro-element modelling (Cassidy et al., 2012; Yang et al., 2012; Peccin da Silva et al., 2021; Peccin da Silva, 2021), and numerical simulations (Al Hakeem and Aubeny, 2019; Choudhary et al., 2018; Evans, 2019). Among these methods, 3D FE analysis allows for detailed anchor-soil interaction modelling under different loading conditions at a relatively low cost. Besides, the local soil response can be investigated in detail to promote the understanding of the anchor-soil interaction mechanisms and help to support plate anchor optimization design from the perspective of laboratory soil element tests. However, few 3D FE studies have been carried out to systematically explore the post-cyclic behaviour of horizontally oriented plate anchors in sand.

Accurate 3D finite element analysis of geotechnical problems relies on the careful selection of a reliable soil constitutive model. The chosen model should possess theoretical accuracy, user-friendliness, and ideally, the ability to precisely capture the behavioral characteristics of diverse soil types. The Cam-clay model (Schofield and Wroth, 1968), regarded as a pivotal advancement in modern soil constitutive modelling, is particularly well-suited for simulating behaviour of normally consolidated clay. By introducing an elegantly defined unified hardening parameter and the Transformed Stress (TS) method into the critical state framework, Yao et al., (2009, 2019) developed the UH (unified hardening) model which can effectively and uniformly capture the three-dimensional (3D) stress-strain characteristics of various types of soils. Some models that only designate for particular soil type, like SANISAND-MS model developed by Liu et al. (2019), has been successfully applied to simulate monopile cyclic behaviour recently (Liu et al., 2020, 2022a, 2022b), demonstrating its potential for use in simulating the response of cyclically loaded offshore structures in sand. The SANISAND-MS model is an elasto-plastic model based on bounding surface theory and critical state framework. The model takes into account the effects of soil fabric effects through a so-called 'memory surface' (Corti et al., 2016) and is proven to be capable of accurately reproducing the cyclic ratcheting behaviour of sand. Afterwards, Lan et al. (2023) upgraded the original SANISAND-MS by employing hyperelasticity law. The updated SANISAND-MS model is featured as a physical adaptation and thermodynamically consistent, without losing the accuracy in reproducing sand cyclic behaviour.

In this work, 3D FE analyses are performed to study the soil-anchor interaction mechanisms, using the upgraded SANISAND-MS constitutive model (Lan et al., 2023). The open source FE platform OpenSees (McKenna, 2011) is selected for this purpose. Since the long-term cyclic environmental loads experienced by floating OWTs usually have low amplitude and frequency (Vorpahl et al., 2013), the post-installation long-term cyclic response of the sandy soil around plate anchors can be assumed as drained. However, one should be aware that the assumption of a drained condition without considering any consolidation effect could underestimate the anchor capacity by 40%, according to previous research (Chow et al., 2020). Parametric studies are conducted to explore the effects of soil relative density, cyclic amplitude

ratio, cyclic asymmetric ratio, embedded depth, anchor geometry, and soil-anchor interface. The local soil response (e.g. element stress and strain) is investigated in detail to gain insights into the local anchor-soil interaction mechanisms. The findings from the study can contribute to the refinement of the laboratory test programs and aid in the detailed design of plate anchors.

2. 3D-FE analysis of soil-anchor interaction

Plate anchor is an efficient solution for mooring offshore floating facilities. Soil-anchor interaction is complex and can greatly affect the stability of floating OWTs. In this study, 3D finite element models of soil-anchor interaction were constructed using the open source platform OpenSees (McKenna, 2011) to systematically explore the monotonic, cyclic and post-cyclic behaviour of horizontally oriented plate anchors, with a particular focus on the cases of plate anchors subjected to vertical loads (which is often the case of plate anchors holding TLPs). Influencing factors such as embedded depths, relative densities, anchor aspect ratios and cyclic load characteristics were considered. The upgraded SANISAND-MS model was employed to capture the small strain nonlinearity and anisotropic features of sand. More importantly, the upgraded SANISAND-MS model can avoid large spurious accumulations of strain under conditions of many loading cycles with small load amplitudes (Lan et al., 2023).

2.1. Geometry and material parameters

Fig. 1 displays the 3D FE model adopted in this work, where L, B and t stand for the length, breadth and thickness of the plate anchor, while H represents the embedded depth of the plate anchor. Due to its symmetry, the quarter model was used to expedite the computation. The plate anchors were modelled as steel using a linear elastic material model. Typical steel material properties of Young's modulus ($E_{steel} = 2.21 \times 10^8$ kPa), Poisson's ratio ($\nu_{steel} = 0.3$) and density ($\rho = 7.85$ g/cm^3) were set for the plate anchor. For the boundary conditions, the bottom surface of the plate anchor was restrained in all directions of the movements, whereas the lateral boundaries were fixed in the normal direction. To eliminate any effects from boundaries, the length and width of the geometric model were always kept larger than $H + L/2$ and $H + B/2$, and the anchor was always placed at a distance greater than $2L$ from the bottom of the model (Choudhary et al., 2018).

The soil domain was assumed to be uniform Karlsruhe quartz sand. The properties of the Karlsruhe quartz sand are as follows: maximum void ratio $e_{max} = 0.874$, minimum void ratio $e_{min} = 0.577$, median particle diameter $D_{50} = 0.55$ mm, uniformity coefficient $C_u = 1.8$, dry unit weight $\gamma = 16.0$ kN/m^3 which corresponds to the relative density of 83% (Wichtmann et al., 2005). The relative densities of 30% and 70% were chosen to represent the loose and dense states, respectively.

2.2. Upgraded SANISAND-MS model

The upgraded SANISAND-MS constitutive model developed by Lan et al. (2023) is adopted to capture the sand's cyclic behaviour. The upgraded SANISAND-MS model is an elasto-plastic model based on bounding surface theory and a critical state framework. The model contains three loci (Fig. 2): (a) a narrow conical yield surface; (b) a wide conical bounding surface; (c) a conical memory surface. The effect of the fabric changing during cyclic loading is considered by the so-called 'memory surface' (Corti et al., 2016; Liu et al., 2019). The state parameter (ψ) is used in the model to unify the treatment of loose and dense sands under one group of constitutive parameters (Dafalias et al., 2004). In the upgraded SANISAND-MS model, the hyperelasticity law proposed by Houlsby et al. (2019) is adopted to ensure that elastic strain does not accumulate upon elastic cyclic loading and thus, to accurately predict strain accumulation under high-cyclic loads. The upgraded
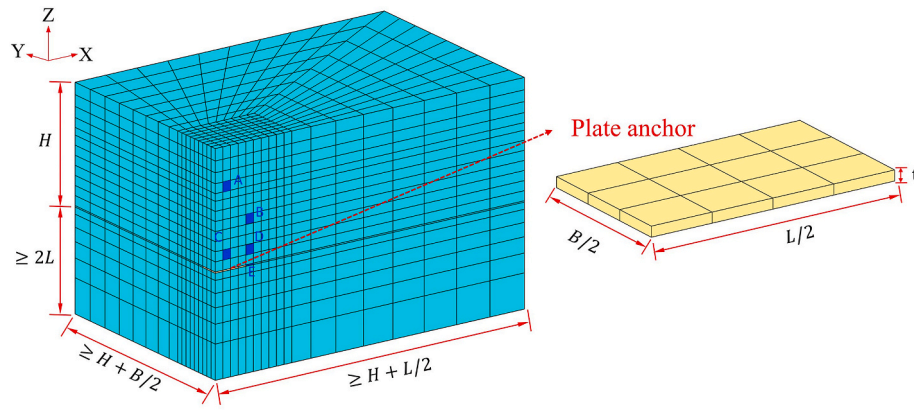
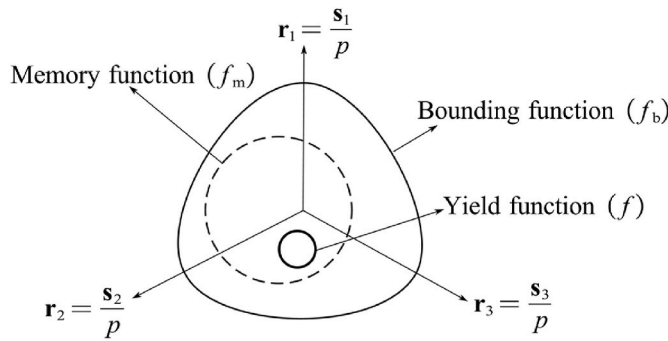**Fig. 1.** 3D finite element model and the geometry of the plate anchor.

Fig. 2. Relevant loci in the deviatoric stress ratio plane (modified after Liu et al., 2019).

SANISAND-MS model contains 18 parameters that can be calibrated against the sand's monotonic and cyclic responses. As shown in Fig. 3, the model parameters of Karlsruhe quartz sand (as presented in Table 1) have been calibrated against laboratory test data performed by Wichtmann et al. (2005). Fig. 3 shows that the predicted stress-strain response of monotonic drained tests and the accumulated total strain of cyclic drained tests agree well with the test results. The calibration procedure can be found in Liu et al. (2019) and Lan et al. (2023) and will not be repeated here.

2.3. FE model settings

The soil domain and plate anchor were modelled by an 8-noded *SSPbrick* element in OpenSees. The 8-noded *SSPbrick* elements ensure the physically stabilized single-point integration, which eliminates

Table 1
Upgraded SANISAND-MS model parameters of Karlsruhe quartz sand calibrated by Lan et al. (2023).

Model features	Parameters	Values
Elasticity	n	0.3
	ν	0.05
	k	330
	y	0.9
Critical state	M	1.27
	c	0.712
	λ_c	0.049
	e_0	0.845
	ξ	0.27
Yield surface	m	0.01
Plasticity modulus	h_0	1.54
	c_h	1.01
	n_b	1.95
Dilatancy	A_0	1.02
	n_d	1.05
Memory surface	μ_0	260
	ζ	0.0005
	β	1

volumetric and shear locking and improves computation precision and efficiency (McGann et al., 2015). For the plate element, the *equalDOF* command enforces equal vertical displacements for all nodes, which prohibits any thickness change in the plate anchor. The *zeroLengthContact3D* command was used to make node-to-node frictional contact between the plate and soil interface, where the penalty method is implemented to control the penetration of two contact nodes through horizontal and vertical stiffness penalties of K_t and K_n, respectively. The
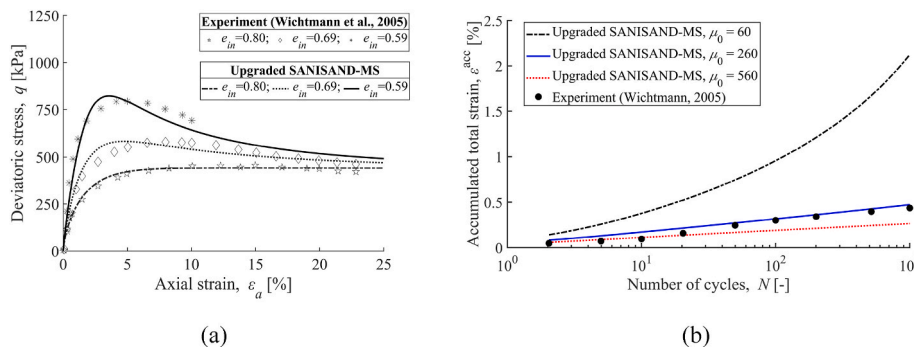

(a)

(b)

Fig. 3. Calibration of model parameters against experimental findings conducted by Wichtmann et al. (2005), (a) triaxial monotonic drained tests under the constant $p_{in} = 200$ kPa, varying e_{in}, (b) triaxial cyclic drained tests following the settings: $e_{in} = 0.702$, $q^{ampl} = 60$ kPa, $p_{in} = 200$ kPa, $\eta^{ave} = 0.75$ (Lan et al., 2023).

soil-anchor interface beneath the plate anchor can be contacted node-to-node by applying the *zeroLengthContact3D* element. This contact allows the interface between the bottom soil and anchor to separate freely when the normal contact stress reduces to zero. Fully binding contact is an alternative method for addressing the soil-anchor interface. When applying fully binding contact, the nodes between the soil and anchor must be bound in all degrees of freedom, and thus there should be no gap at the base of the plate anchor during the pullout process.

The installation process of the plate anchor was not simulated, and the plate anchor was assumed to be wished in place before applying vertical load in this study. The stiffness penalties (K_t and K_n) at the soil-anchor interface were set sufficiently high to prevent the nodes of the plate anchor and the nodes of the soil elements from penetrating each other (Balomenos et al., 2020). Other input parameters to the *zeroLengthContact3D* element are cohesion (c_z) and friction coefficient (μ). Since the soil domain was modelled as sand, the cohesion (c_z) coefficient is set to zero. To test the effect of the friction coefficient (μ) on the load-displacement response of plate anchors, three simulations associated with loose sand were performed with different values of μ (0.1, 0.4, and 0.7). All other parameters, as presented in Tables 1 and 2, were kept the same. The three simulations were performed on anchors with the following dimensions: $H/B = 3$, $L/B = 1.7$, $B = 4.64$ m, and $t = 0.6$ m. The vertical monotonic load was applied at the centroid of the upper surface of the plate anchor. As shown in Fig. 4, despite the increase in the value of μ, the load-displacement response remains nearly identical. This indicates that, for a horizontally oriented plate anchor subjected to vertical loading, the frictional effect at the anchor-soil interface is not significant. Therefore, a value of $\mu = 0.7$ was selected for this study. The selected parameters for the *zeroLengthContact3D* element are shown in Table 2.

2.4. Mesh size effect

A convergence study was carried out to test the meshing effect in a loose sand domain. Fig. 5(a)–(d) show four FE models with 1976, 3306, 4598, and 7524 elements, respectively. Frictional contact elements (which will be discussed in Section 3.1.1) were employed in the four FE models to model the soil-anchor interface.

The vertical monotonic load was applied at the centroid of the upper surface of the plate anchor. The load was applied until a normalized vertical displacement of $\delta_z/B = 5\%$ was achieved, where δ_z stands for the vertical displacement of the plate anchor at the loading point and B is the breadth of the plate anchor. Fig. 6 displays the results of the FE simulation with different mesh sizes. There is a trend that finer mesh results in larger vertical displacement under the same uplift load. At the same time, with the difference of 3.1% in the simulated uplift load when using 4598 and 7524 elements at $\delta_z/B = 5\%$, a clear convergence trend was observed upon mesh refinement. To reach a balance between accuracy and computational efficiency, the 4598-element model (Fig. 4 (c)) was used in the following sections.

2.5. Simulation programme

The vertical pullout resistance of the horizontal plate anchor was simulated in 3D finite element analysis with both monotonic and cyclic loads applied. The load-displacement curves obtained from the monotonic up-lifting simulations were used to determine the ultimate pullout capacity of the corresponding plate anchor. Various criteria have been proposed for determining the ultimate pullout capacity, e.g., the specific
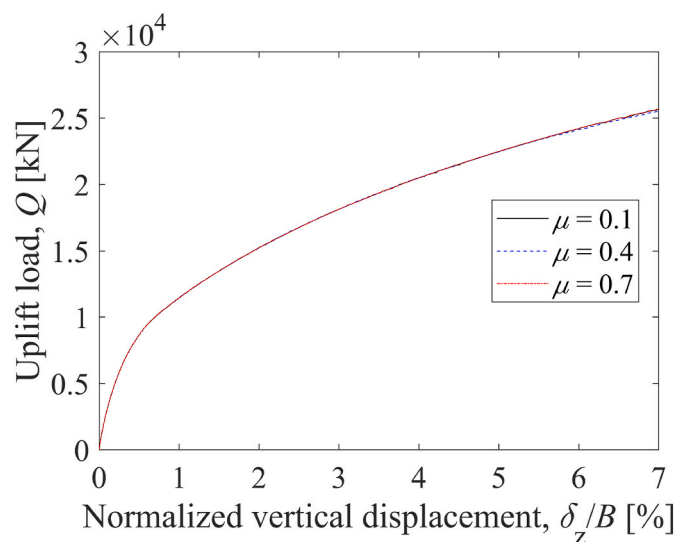

Fig. 4. The influence of friction coefficient (μ) on vertical load-displacement curves at the load point.

displacement criterion (Vesić, 1973), the double tangent intersection criterion (Boushehrian et al., 2009), the function fitting criterion (Ghaly, 1997; Hanna et al., 2007) and 'K4' criterion (Rowe and Davis, 1982). In this work, the specific displacement criterion was used to determine the ultimate pullout capacity of the plate anchor. That is, taking ultimate pullout capacity as the pullout load corresponding to a certain value of δ_z/B (in this case, 5% is selected).

To investigate the load-displacement behaviour of the plate anchor subjected to vertical cyclic loading, the one-way cyclic loads (loading program sketched as in Fig. 7) were applied under control of cyclic amplitude ratio ζ_b and cyclic asymmetric ratio ζ_c. ζ_b and ζ_c are defined the same as in LeBlanc et al. (2010):

$$\zeta_b = \frac{F_{max}}{F_{ref}} \tag{1}$$

$$\zeta_c = \frac{F_{min}}{F_{max}} \tag{2}$$

where F_{max}, F_{min} stand for maximum and minimum vertical load in a load cycle, respectively. F_{ref} is the reference vertical load that causes a given reference vertical displacement of the plate anchor. In general, F_{ref} is selected to be the monotonic ultimate pullout capacity.

Table 3 summarizes the test plans for cyclic numerical simulation. 14 numerical simulation tests were conducted on dense and loose sand with ζ_b in the range of 0.1–0.45, the tests involved cyclic one-way loading only with ζ_c in the range of 0~0.5. Since the step-by-step analysis of high-cyclic soil–structure interaction is computationally prohibitive (Liu et al., 2019), the number of cycles was limited to 100. On a computer equipped with an Intel i7-9700K CPU with a base frequency of 3.6 GHz, it takes approximately 29~85 h to calculate each of the cyclic cases listed in Table 3. At the end of the 100th cycle, a monotonic pullout stage (post-cyclic stage) was added to investigate the post-cyclic behaviour of the plate anchor. The monotonic pullout load in the post-cyclic stage was applied until the vertical displacement of the plate anchors at the post-cyclic stage reaches $\delta_z/B = 6\%$. The initial relative densities $D_{r,in} = 30\%$ and $D_{r,in} = 70\%$ were set before the application of the gravity loading stage. Thus, at the beginning of the vertical loading stage, the relative densities in soil domain slightly increased.

3. Numerical results

In this section, 3D FE simulation results of monotonic loading are

Table 2
The parameter settings of *zeroLengthContact3D* element.

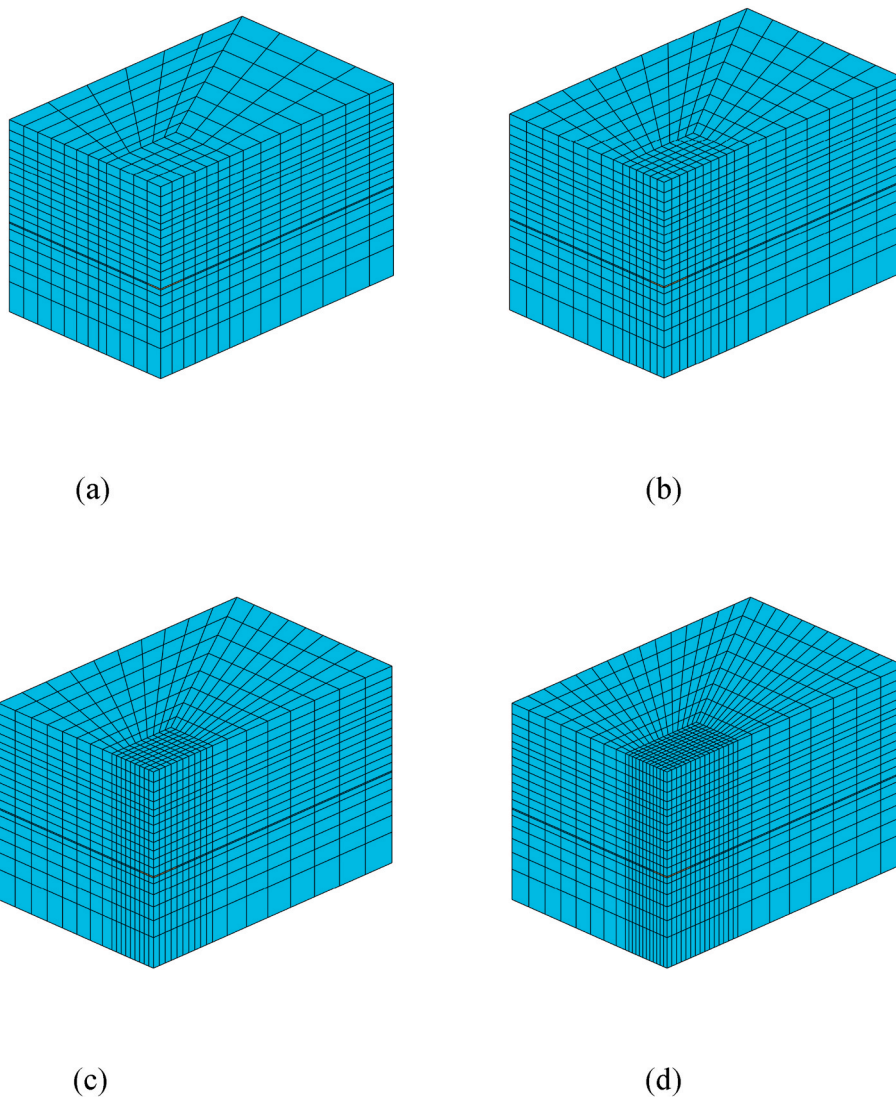| K_n	K_t	μ	c_z
1.0×10^{12}	1.0×10^{12}	0.7	0.0

(a)

(b)

(c)

(d)

Fig. 5. Auxiliary models for sensitivity analysis of mesh size effect: (a) 1976 elements; (b) 3306 elements; (c) 4598 elements; (d) 7524 elements.
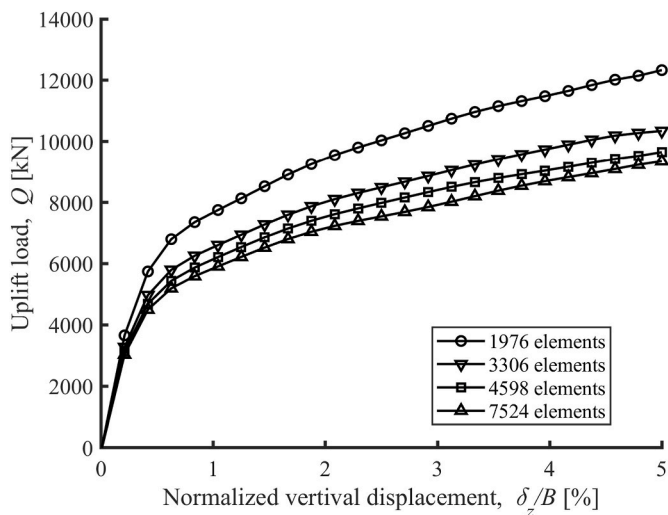

Fig. 6. The influence of mesh size on vertical load-displacement curves at the load point.
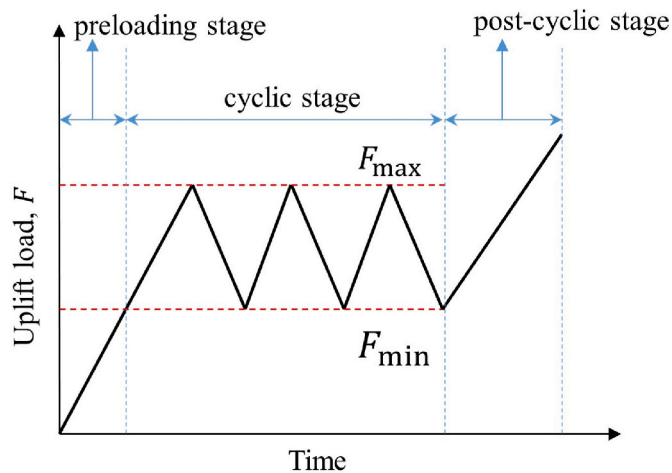

Fig. 7. Illustration of the loading sequence considered in cyclic tests.

first presented to study the influence of sand's relative density, soil-anchor interface, aspect ratio, and embedded depth ratio on the monotonic behaviour of the plate anchor. After that, the results of cyclic

Table 3
The details of numerical simulation cases for cyclic tests.

Test label	$D_{r,in}$	ζ_b	ζ_c	Test label	$D_{r,in}$	ζ_b	ζ_c
L1	30%	0.45	0.50	D1	70%	0.45	0.50
L2	30%	0.30	0.50	D2	70%	0.30	0.50
L3	30%	0.10	0.50	D3	70%	0.10	0.50
L4	30%	0.40	0.50	D4	70%	0.40	0.50
L5	30%	0.40	0.30	D5	70%	0.40	0.30
L6	30%	0.40	0.10	D6	70%	0.40	0.10
L7	30%	0.40	0	D7	70%	0.40	0

loading are analyzed to explore the effect of cyclic characteristics (ζ_b and ζ_c) on the cyclic behaviour of the plate anchor, specifically for the post-cyclic uplift load resisted by plate anchors and vertical displacement accumulation. Finally, the soil states around the plate anchor are studied at element level.

3.1. Monotonic behaviour

3.1.1. Effect of soil-anchor interface

For an anchor's uplift test, it is common to observe the collapse of sand into the gap created beneath the anchor (Dickin and Laman, 2007). This phenomenon indicates that the anchor and soil are separating during the uplift process, resulting in the formation of a gap beneath the anchor. In this study, two types of contacts are used at the base of the plate anchor to investigate the effect of gap on the bearing characteristics of a plate anchor, as indicated in Fig. 8, where monotonic uplift loads were applied to the model with $H/B = 3$, $L/B = 1.7$, $B = 4.64$, and $t = 0.6$ m for loose sand.

Fig. 8 illustrates color maps of vertical displacement for loose soil when $\delta_z/B = 5\%$ at the loading point. As shown in Fig. 8(a), the soils beneath the plate anchor are pulled up with the uplifting of the anchor, as the soil-anchor interface is assumed to be fully binding with no gap allowed. Whereas, in Fig. 8(b), due to the use of a frictional contact interface, a gap between soil and anchor can be simulated (a large scale of the gap is shown in Fig. 8(c)). The frictional contact interface was simulated using *zeroLengthContact3D* element. As a result, the soil beneath the anchor was not significantly heaved but showed a slight rebound instead. The lateral and upper interfaces of the plate anchor

were assumed to be fully binding contacts for both cases.

Fig. 8 demonstrates that the vertical displacement of the soil is concentrated in a bubble-shape zone above the plate anchor, which extends towards the ground surface. This pattern suggests a shallow failure pattern. A similar failure pattern for embedded ratio $H/B = 3$ has been reported by Choudhary et al. (2018) from the 3D FE analysis of a square plate anchor.

The normalized vertical load-displacement responses of the loading point for loose and dense sand with two types of contacts are presented in Fig. 9. As shown in Fig. 9, the load-displacement curves for loose or dense sand have a similar trend regardless of whether a soil-anchor interface separation is allowed or not. When the vertical displacement is small ($\delta_z/B = 0 \sim 0.3\%$), the load-displacement responses of all cases are nearly identical. As the load increases, the difference among the four curves gets larger. White et al. (2008) have demonstrated that the uplift capacity of the plate anchor is comprised of two resistant components: (a) the upper covered weight of soils and the weight of the plate anchor,
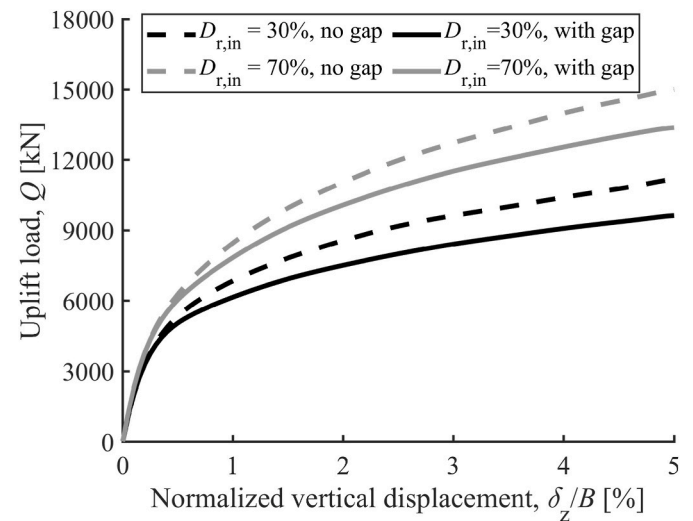
Fig. 9. Normalized vertical load-displacement responses at the loading point.
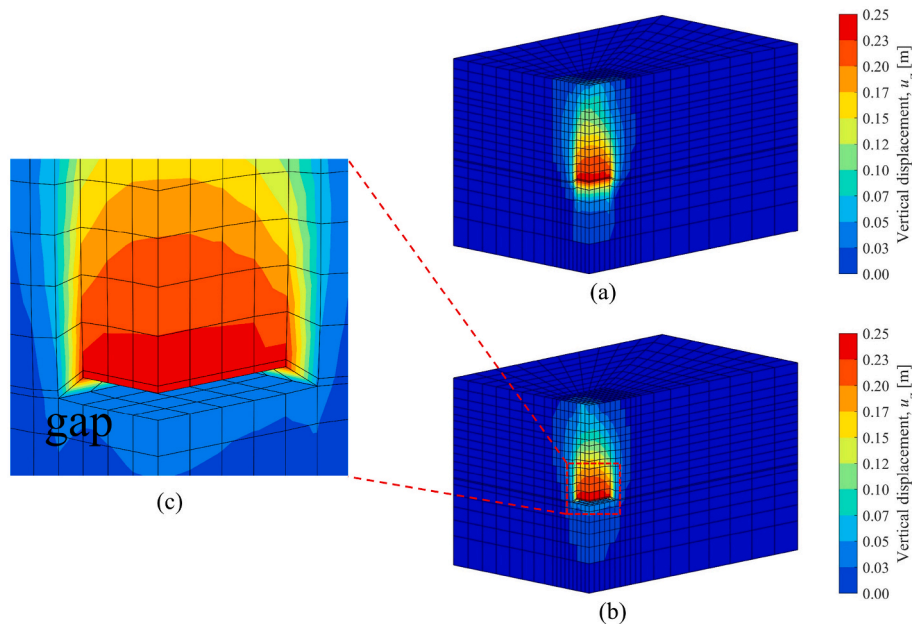
Fig. 8. Distribution of vertical displacement of soil when the $\delta_z/B = 5\%$ at the loading point. (a) $D_{r,in} = 30\%$, with no gap allowed, (b) $D_{r,in} = 30\%$, with gap allowed, (c) local large scale of gap.

(b) the shear strength of the soil along the sliding band above the plate anchor. In comparison to the loose sand, the dense sand has greater shear resistance along the shear surface, resulting in a greater uplift load, as shown in Fig. 9. When the normalized vertical displacement $\delta_z/B = 5\%$, the uplift load of the dense sand case is 38.9% and 34.1% higher than that in the loose sand case, respectively, under the circumstances of with and without a gap, respectively. The uplift load is affected by the presence of gaps. As illustrated in Fig. 9, in loose sand, the uplift load is 12.2% higher when gaps are not permitted in the simulation settings. In dense sand, the number is 16.1%. The reason for this is that when the soil-anchor interface is set by fully binding contact, the shear strength of the soil below the plate anchor can be mobilized and contribute to generating resistance.

3.1.2. Effect of embedded depth ratio (H/B)

Three different embedded depth ratios (H/B=1, 3 and 5) were simulated to investigate the influence of embedment depth on the anchor's bearing characteristics in loose and dense sand. Frictional contact is adopted at the soil-anchor interface in this section, which allows the anchor and soil to separate freely when the normal contact stress reduces to zero. The width (B) and thickness (t) of the plate anchor are fixed at 4.64 m and 0.6 m, respectively (the same value as indicated in Section 3.1.3) and the aspect ratio (defined as L/B) was set to 1.7. Monotonic uplift loads were applied at the centroid of the upper surface of the plate anchor.

The load-displacement curves for different embedded depth ratios $H/B = 1$, 3 and 5 and initial relative densities $D_{r,in} = 30\%$ and 70% are demonstrated in Fig. 10(a). For both dense and loose sand, an increase in the H/B results in a greater uplift load Q. The variations of Q with H/B for loose and dense sand are plotted in Fig. 10(b), which is accomplished by extracting the uplift load Q that triggers normalized vertical displacement $\delta_z/B = 3\%$. The Q increases almost linearly with increasing H/B. Similar linear trends of the uplift load as a function of H/B are reported in Rowe and Davis (1982) based on physical modelling results, in Merifield and Sloan (2006) by numerical limit analysis, and in Evans (2019) by discrete element method (DEM). Fig. 11 displays color maps of the distribution of vertical displacement for $H/B = 1.0$ and 3.0, respectively. It can be seen that a larger embedment depth ratio implies greater soil weight above the anchor and a longer sliding surface, resulting in a higher Q.

As illustrated in Fig. 10, for a given H/B, the uplift load of a plate anchor in dense sand is larger than the one in loose sand. As H/B increases, the disparity between uplift loads in loose and dense sand increases. In Fig. 10(a), the load-displacement curves are almost identical for loose and dense sand when $H/B = 1$, but they vary for larger H/B ratios (e.g., the cases with $H/B = 3$ and $H/B = 5$, which are relevant for floating offshore structures). As can be seen in Fig. 10(b), the uplift load of the plate anchor appears to converge to the same value for both loose

and dense sand with a small embedded depth ratio. Similar conclusions have been reported by Schofield and Wroth (1968) and Liang et al. (2021). Fig. 11(a)~(d) compare the vertical displacement distribution for loose and dense soil at shallow embedment ($H/B = 1.0$) and deeper embedment ($H/B = 3.0$), respectively. The color maps for the shallow embedment depth ($H/B = 1.0$) reveal that the size of the influence zone at loose and dense sand is almost the same, except that the horizontal extension of the ground is slightly wider in dense sand. Fig. 11(c) and (d) show that for deeper embedment depth $H/B = 3.0$, in the case of loose sand, the mobilization zone is in a bubble-shape. In the case of dense sand, a conical-shape mobilization zone is formed.

3.1.3. Effect of aspect ratio (L/B)

Six simulations were run with three different aspect ratios ($L/B = 1.7$, 2.5, and 3.5) in both loose and dense sand to examine the impact of anchor geometry on the bearing characteristics of the plate anchor. The soil-anchor interface was set to allow a gap to occur. The embedded depth ratio (H/B) was set at 3.0.

Fig. 12(a) shows the uplift load Q versus the normalized vertical displacement δ_z/B for each aspect ratio in both dense and loose sand. As the geometry of the anchor becomes larger, more soil is mobilized, resulting in an increase in the uplift load. Take the Q corresponding to $\delta_z/B = 3\%$ to study the influence of L/B on the uplift load. For the plate anchor with $L/B = 1.7$, the uplift load $Q_{L/B=1.7} = 8411$ kN for loose sand, and $Q_{L/B=1.7} = 11517$ kN for dense sand. Dickin and Laman (2007) performed centrifuge tests on 25 mm wide, 3 mm thick stainless steel model anchor plates with aspect ratios $L/B = 1$, 2, 5, and 8 in sand. The normalized uplift load $Q/Q_{L/B=1.7}$ in this study is compared with the experimental results conducted by Dickin and Laman (2007). Fig. 12(b) demonstrates that the uplift load increases almost linearly as the aspect ratio increases. The difference in slope is due to the different soil types and soil densities, among other factors.

3.2. Cyclic behaviour

Horizontally orientated plate anchors are subjected to vertically cyclic wave and current loads when they are used to secure TLPs. In this section, cyclic vertical loads were applied to the plate anchor, and the cyclic behaviour of the sand was modelled using the upgraded SANISAND-MS model. The details and model parameters for the upgraded SANISAND-MS model have been introduced in the previous section. The investigation focuses on the factors of the cyclic amplitude ratio ζ_b and the cyclic asymmetric ratio ζ_c, which are listed in Table 3. The cyclic uplift load is applied in a manner as sketched in Fig. 7. The number of cycles was limited to $N = 100$. After cyclic loading, the plate anchor is monotonically loaded until the vertical displacement δ_z/B range at the post-cyclic stage reaches 6%. The soil-structure model is defined with the embedded depth ratio $H/B = 3.0$, anchor width $t = 0.6$
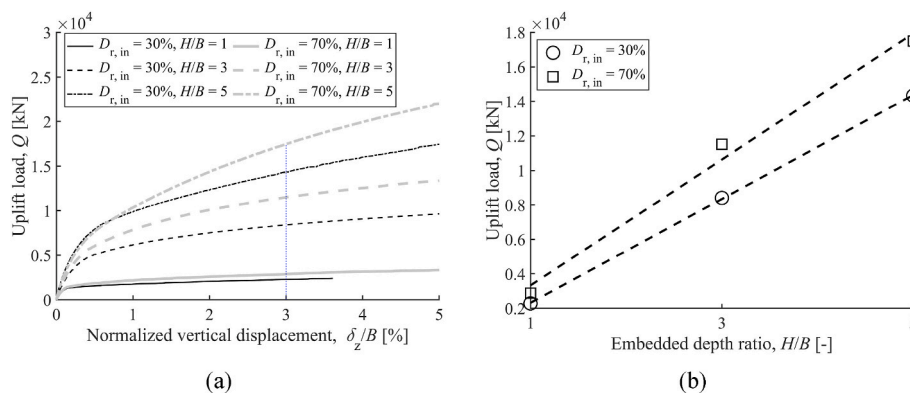

(a)   (b)

Fig. 10. Influence of embedded depth ratio (H/B) on anchor's uplift bearing behaviour under a constant $L/B = 1.7$. (a) Variation of uplift load with normalized vertical displacement for different H/B and initial relative densities, (b) variation of uplift load with H/B when $\delta_z/B = 3\%$.
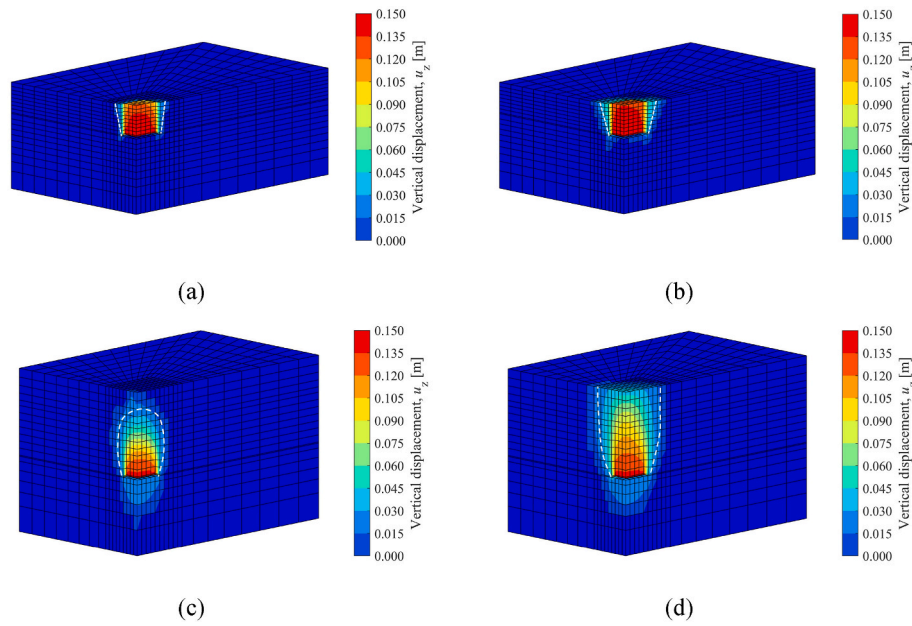
Fig. 11. Distribution of vertical displacement when the δ_z/B of the loading point is equal to 3% with the setting of $L/B = 1.7$. (a) $D_{r,in} = 30\%$, $H/B = 1.0$, (b) $D_{r,in} = 70\%$, $H/B = 1.0$, (c) $D_{r,in} = 30\%$, $H/B = 3.0$, (d) $D_{r,in} = 70\%$, $H/B = 3.0$.
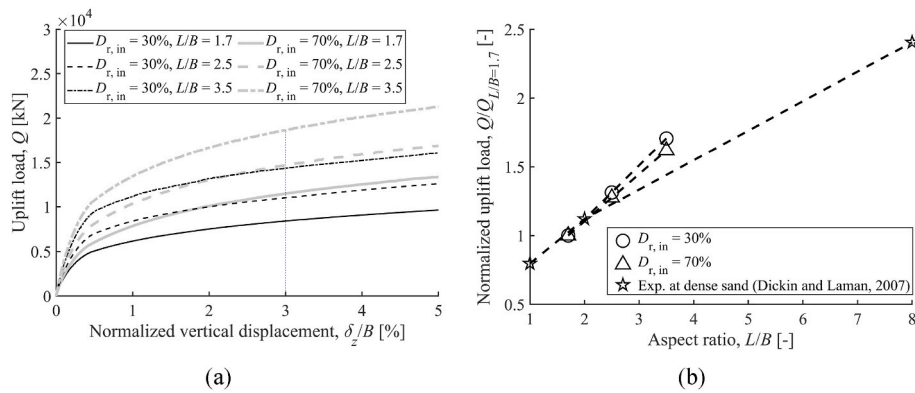

Fig. 12. Influence of aspect ratio (L/B) on anchor's uplift bearing behaviour under a constant $H/B = 3$. (a) Variation of uplift load with normalized vertical displacement for different L/B and initial relative densities, (b) variation of uplift load with L/B when $\delta_z/B = 3\%$.

m, and the aspect ratio of the plate anchor of $L/B = 1.7$, and the soil-anchor interface is set to allow a gap to occur.

3.2.1. Effect of cyclic amplitude ratio (ζ_b)

To study the impact of ζ_b on the cyclic behaviour of the plate anchor, a 3D FE model was employed. The model was subjected to three different cyclic loads, with $\zeta_b = 0.1$, 0.3 and 0.45, while maintaining the
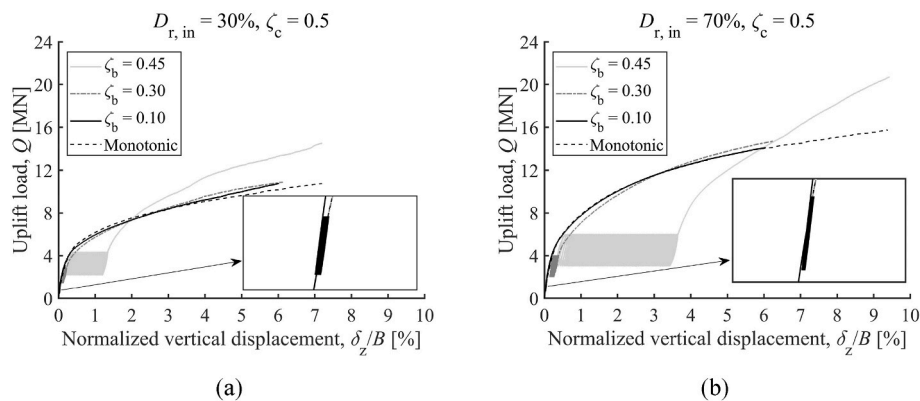

Fig. 13. Uplift load-displacement curves for different ζ_b under a constant $\zeta_c = 0.5$. (a) In loose sand with $D_{r,in} = 30\%$, (b) in dense sand with $D_{r,in} = 70\%$.

same $\zeta_c = 0.5$. Fig. 13 displays the cyclic load displacement curves of the plate anchor in both loose sand and dense sand conditions. As shown in Fig. 13, when the cyclic amplitude is small (e.g., the cases with $\zeta_b = 0.1$), there is a very small displacement accumulation of the plate anchor during cyclic loading. As the cyclic load amplitude increases and becomes sufficiently large to counteract the weight of the plate anchor and a part of the soil, larger displacement accumulations are observed during the initial cyclic stages. For the test with $\zeta_b = 0.45$, the uplift displacement of the anchor occurs in the first few cycles. Subsequently, the rate of displacement accumulation decreases.

After the cyclic stage, monotonic loading was applied to examine the post-cyclic uplift characteristics of the plate anchor. As shown in Fig. 13, during the post-cyclic stage, the load-displacement response of tests that underwent a previous cyclic stage exhibits a similar trend to that of tests without cyclic loading (monotonic tests), in which the uplift load increases with an increase in displacement. Nevertheless, cyclic loading leads to a higher post-cyclic uplift load compared to monotonic tests in both loose and dense sand. The post-cyclic uplift load increases more in tests with a high cyclic amplitude ratio ζ_b. The only exception is the case of plate anchor in dense sand where $\zeta_b = 0.1$ was applied, in this case, almost no cyclic effects were observed in this case. Another observation is that the relative density does not significantly influence the cyclic loading on the post-cyclic uplift load. For example, in the case of $\zeta_b = 0.45$, the post-cyclic uplift load in loose sand is 35.3% (in dense sand it is 31.4%) greater than the load observed under the monotonic loading when the range of post-cyclic displacement reaches $\delta_z / \mathrm{B} = 6\%$. Similar overshooting of the load-displacement response has been reported in Chow et al. (2015) through experimental studies and in Evans (2019) through numerical simulation.

To elucidate the mechanism behind the increased uplift load during post-cyclic loading, color maps depicting the relative density (D_r) of the soil domain at the end of the 100th cycle are shown in Fig. 14. In Fig. 14, it is observed that the relative density of the soil around the plate anchor increases after 100 cycles. This increase in relative density indicates that the soil around the plate anchor undergoes densification as a result of cyclic loading. The densification of the sand leads to an increase in the shear strength and stiffness of the soil domain. Consequently, the uplift load experienced by the plate anchor during the post-cyclic stage exceeds the uplift load observed in the monotonic loading case.

Fig. 14 (a) and (b) demonstrate that the degree of sand densification varies between loose and dense sand under identical conditions. Additionally, the area with the highest level of densification is predominantly concentrated in the upper portion of the plate anchor. To investigate the densification of the soil domain in more detail, three horizontal slices are taken below the plate anchor (at the depth of $1B$) and above the plate anchor (at distances of $0.5B$ and $1B$), as indicated by the dashed line in Fig. 14(a). These slices are analyzed separately for both loose and dense sand conditions. Fig. 15 displays the contour of the distribution of the relative density increment ΔD_r at the end of the 100th cycle. The relative

density increment is defined as $\Delta D_r = (D_r - D_{r,in})/D_{r,in} \times 100\%$, where $D_{r,in} = 30\%$ in Fig. 15(a)~(c), and $D_{r,in} = 70\%$ in Fig. 15(d)~(f). In Fig. 15, the rectangular area surrounding the original point indicates the scope of the plate anchor. From Fig. 15(a) and (c), it can be observed that in loose sand, the densification is more pronounced above the plate anchor compared to below it at the same distance of $1B$. In Fig. 15(a), the ΔD_r is approximately 8.5%, whereas in Fig. 15(c), it is almost 15%. In contrast, the range of ΔD_r for dense sand in the same zone of soil domain is between 2.95% and 3.3% in Fig. 15(d) and between 2% and 3.5% in Fig. 15(f). This indicates that, in dense sand, the degree of densification above or below the anchor at a distance of $1B$ is comparable.

As the distance between the slice and the plate anchor increases, the degree of densification decreases. Fig. 15(b) and (c) illustrate that, for the same location, $\Delta D_r \approx 18\% \sim 25\%$ for the case above the plate anchor with $0.5B$, while ΔD_r is about 8%~15% for the case above the plate anchor with $1B$. The initial relative density of sand also influences the degree of densification within the soil domain. As shown in Fig. 15(b) and (e), for a given soil location, the relative density can increase by as much as 25% in loose sand, but by only 5% in dense sand.

Fig. 16 illustrates the distribution of mean effective stress (p) for cases L2 and D2 after 1, 10, and 100 cycles. For a small number of loading cycles ($N = 1,10$), the distribution of p is almost identical for both loose and dense soil. However, as the number of cycles increases, discrepancies between loose and dense soil occur due to load redistribution during cyclic loading. The discrepancies are evident in Fig. 16(e) and (f) for cases with $N = 100$.

For cases L2 and D2, the mean effective stress below the plate anchor decreases with an increasing number of cycles. Initially, the soil beneath the plate anchor is subjected to both the weight of the plate anchor and the soil above it when the cyclic uplift load is initiated. During cyclic loading, the plate anchor gradually rises vertically, as shown by the load displacement curves depicted in Fig. 13(b). With an increasing number of cycles, the applied uplift load gradually balances the weight of the plate anchor and the soil above it. As a result, the mean effective stress beneath the plate anchor decreases, and it may even reduce to zero as the soil and plate anchor are detached.

As depicted in Fig. 16(a), (c) and (e), the distribution of p in zone 1 (directly above the plate anchor) remains between 120–160 kPa as the number of cycles increases. This indicates that the mean effective stress of zone 1 is largely unaffected by the number of cycles in loose sand. However, in dense sand, the mean effective stress above the plate anchor progressively increases with an increasing number of cycles. For example, the mean effective stress in zone 1 starts with the range of 120~160 kPa (Fig. 16(b), but eventually increases to 180–220 kPa at the end of 100 cycles (see Fig. 16(f). In both loose sand and dense sand (cases L2 and D2), the mean effective stress in zone 2 (on the side above the plate anchor) decreases. However, the extent of the decreased mean effective stress is greater in loose sand compared to dense sand, as indicated by the color bar. The decrease in mean effective stress p can be

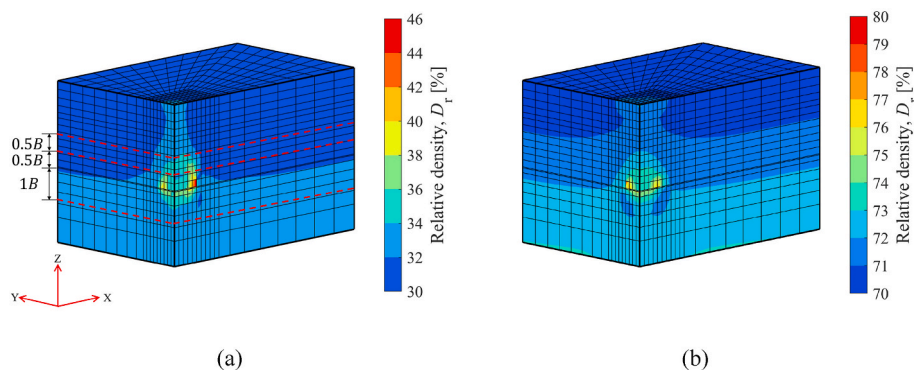(a)   (b)

Fig. 14. Distribution of relative density at the end of the 100th cycle under the settings: $\zeta_b = 0.3$, $\zeta_c = 0.5$. (a) At loose sand with $D_{r,in} = 30\%$, (b) at dense sand with $D_{r,in} = 70\%$.
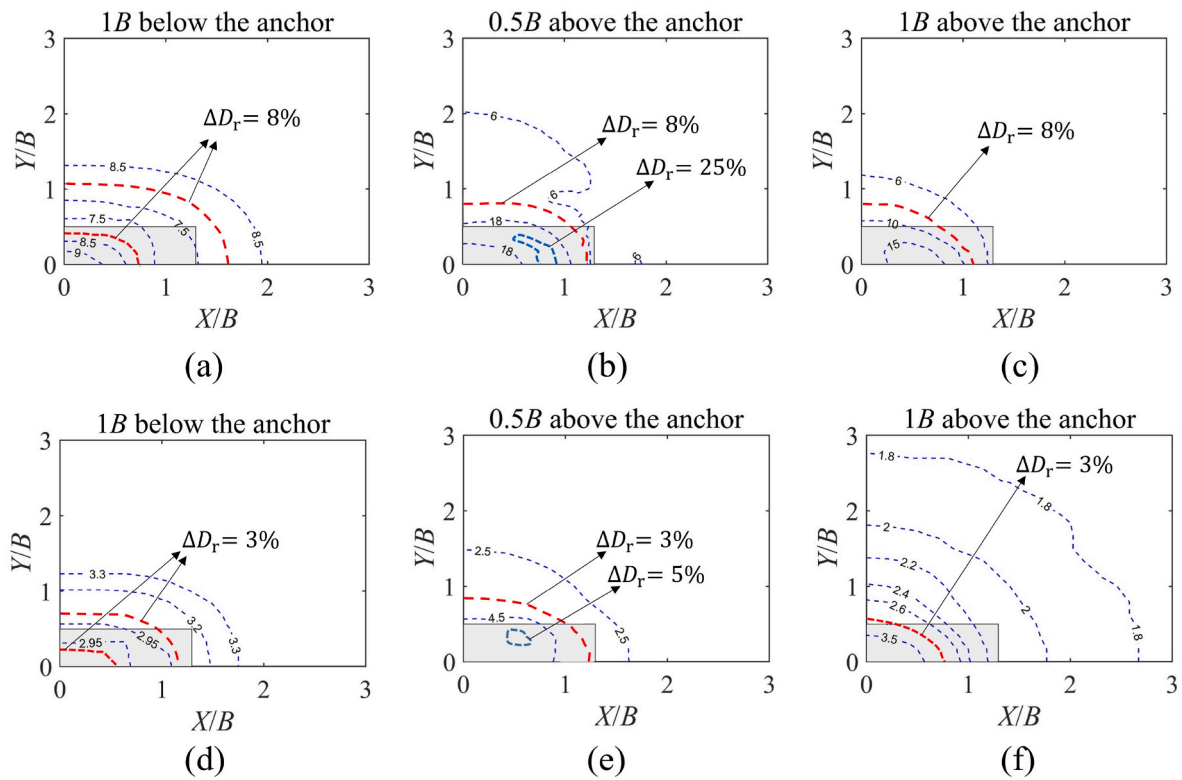
Fig. 15. The contour distribution of the relative increment of relative density $\Delta D_r = (D_r - D_{r,in})/D_{r,in} \times 100\%$ at the end of 100 cycles for (a)~(c) case L2 with $D_{r,in} = 30\%$, and (d)~(f) case D2 with $D_{r,in} = 70\%$.

attributed to two main reasons: (a) load redistribution of the entire soil domain during cyclic loading, and (b) shearing in zone 2 happens with a decreasing volumetric strain rate when the number of loading cycles gets larger, approaching a state of constant-volume shearing conditions. Similar responses of such an approaching state of constant-volume shearing of sands under cyclic loading have been reported by Tsuha et al. (2012) through laboratory tests and by Liu et al. (2022a) with 3D FE simulations. The local soil response (mainly described in Section 3.3) provides evidence supporting the second reason (b). Taking element D (located in zone 2 as shown by Fig. 1) as an illustration, Fig. 24(e) demonstrates that the volumetric strain ε_v increased by 0.61% (from 0.87% to 1.48%) when the number of cycles increases from 60 to 80. However, when N increases from 80 to 100, the volumetric strain increases by only 0.31% (from 1.48% to 1.79%). During the latter part of cyclic loading, the rate of change of volumetric strain in loose sand decreases. On the other hand, in dense sand, as shown in Fig. 24(f), there is only a 0.02% (from 0.43% to 0.45%) increase in ε_v when N changes from 60 to 80, compared to a 0.16% (from 0.45% to 0.61%) increase when N increases from 80 to 100. The change rate of volumetric strain in dense sand increases as the number of cycles increases. Consequently, the degree of p reduction is greater in loose sand than in dense sand.

3.2.2. Effect of cyclic asymmetric ratio (ζ_c)

The influence of the cyclic asymmetric ratio ζ_c on the cyclic behaviour of the plate anchor has been investigated using cases L4~L7 for loose sand and D4~D7 for dense sand (Table 3). The cyclic amplitude ratio (ζ_b) is fixed at 0.4. Fig. 17(a) and (b) present the cyclic load-displacement response for loose and dense sands, respectively. In all the cyclic loading cases shown in Fig. 17, the post-cyclic uplift load is eventually higher than the monotonic uplift load. For loose sand cases, the cyclic asymmetric ratio ζ_c has little effect on the post-cyclic uplift load of the plate anchor. For example, when the range of δ_z / B of post-cyclic stage reaches 6%, the uplift loads of cases L4~L7 exhibit a small range (11.7–12.8 MN). In the case of dense sand, the post-cyclic uplift

load remains similar except for the case with $\zeta_c = 0.1$, as observed for the cases with $\zeta_c = 0.0$, $\zeta_c = 0.3$, and $\zeta_c = 0.5$ at the final of the post-cyclic stage. For the case of $\zeta_c = 0.1$, there is an approximate increase of 10.2 MN in the final post-cyclic load compared to the case of monotonic loading.

Furthermore, it can be observed from Fig. 17(a) that in loose sand – in cases of L6 and L7 with $\zeta_c = 0$ and 0.1, the vertical displacement of the plate anchor is less than zero after cyclic loading, as also shown in Fig. 18(a) that $(\delta_z - \delta_0)/B < 0$. To investigate the influence of ζ_c on vertical displacement accumulation, Fig. 18 presents the normalized vertical displacement of the plate anchor as a function of the number of loading cycles for different ζ_c values, while keeping $\zeta_b = 0.4$. The results show that the regime of vertical displacement accumulation is different between loose and dense sand. In loose sand (Fig. 18(a)), the anchor initially experiences rapid settlement before reaching a stable state when ζ_c is small ($\zeta_c = 0~0.3$). As ζ_c increases, the rate of settlement decreases, and the vertical displacement eventually accumulates in a positive direction. On the other hand, in dense sand, as shown in Fig. 18 (b), the vertical displacement of the plate anchor accumulates upward during cyclic loading. The effect of gravity from the overlying soil and the plate anchor plays an important role when an excessive uplift load is unloaded, resulting in the accumulation of vertical displacement in the opposite direction. It is observed that in loose sand, for a given number of loading cycles, the normalized vertical displacement increases with an increase of ζ_c. Similarly, in dense sand, an increasing trend in normalized vertical displacement is observed in Fig. 18(b) as ζ_c changes from 0 to 0.3. However, the normalized vertical displacement in dense sand decreases when ζ_c increases to 0.5.

3.3. Local soil response

When a plate anchor is subjected to cyclic loading, it may induce stress and strain variations in the soil surrounding the anchor. Understanding the local soil behaviour around the anchor is essential for
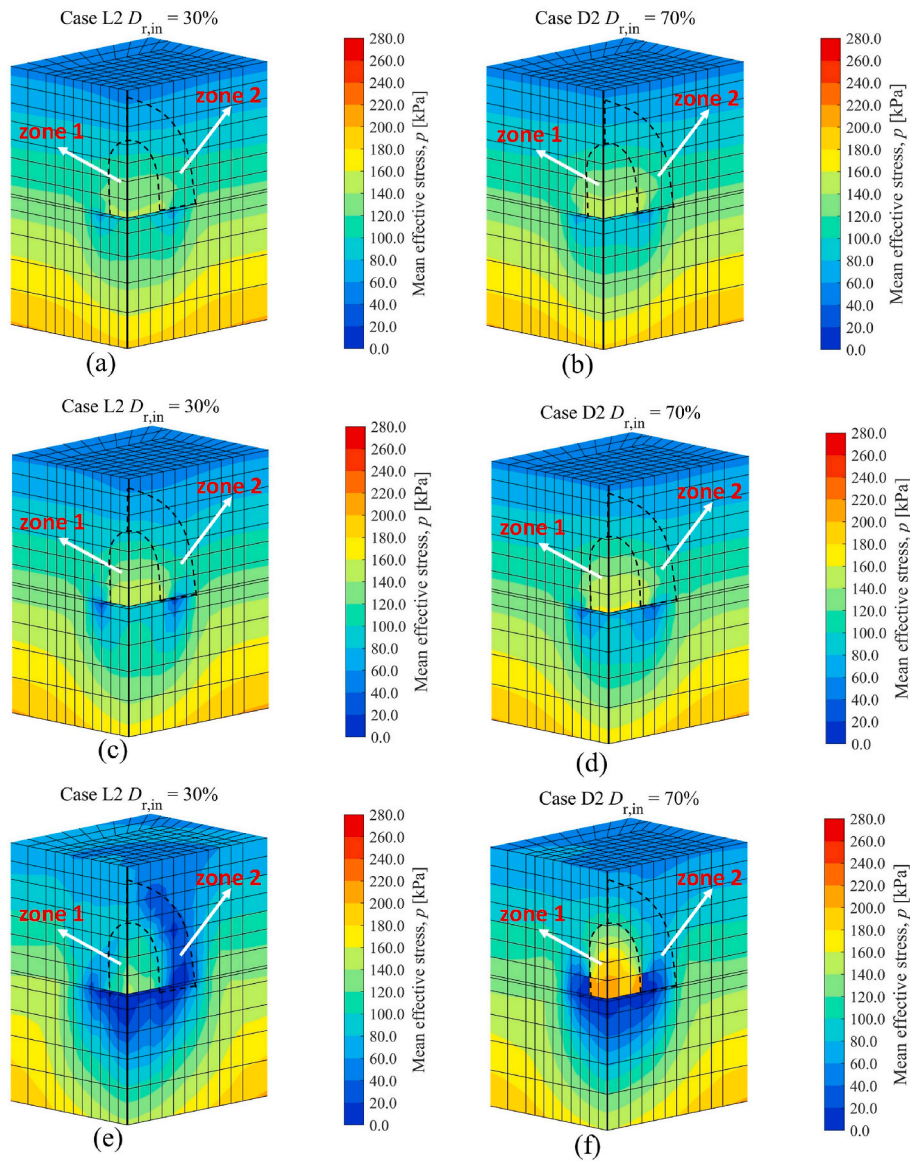
Fig. 16. Distribution of mean effective stress p in loose and dense sand at the end of (a)~(b) 1 cycle, (c)~(d) 10 cycles, (e)~(f) 100 cycles.
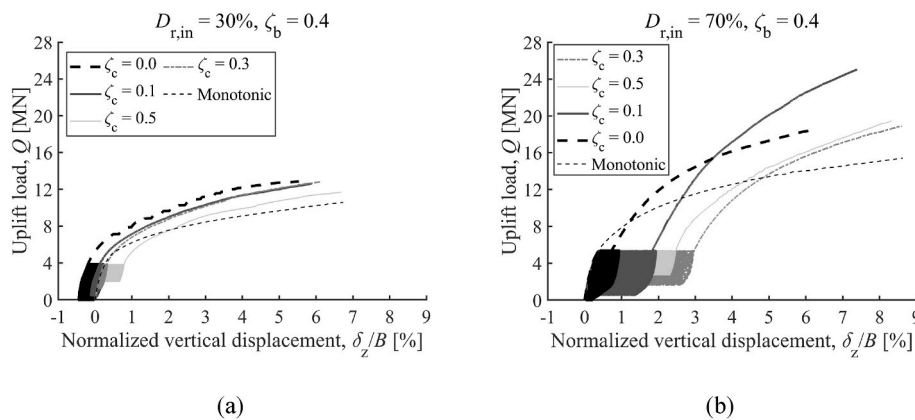

Fig. 17. Uplift load-displacement curves for different ζ_c under a constant $\zeta_b = 0.4$. (a) In loose sand with $D_{r,in} = 30\%$, (b) in dense sand with $D_{r,in} = 70\%$.

optimizing the design of a plate anchor, particularly from a laboratory testing perspective. It is convenient to extract the element stress/strain response at each step of cyclic loading, which aids in comprehending the

local soil behaviour.

In this study, representative elements denoted by A~E (as shown in Fig. 1) were selected to investigate the local soil response. According to
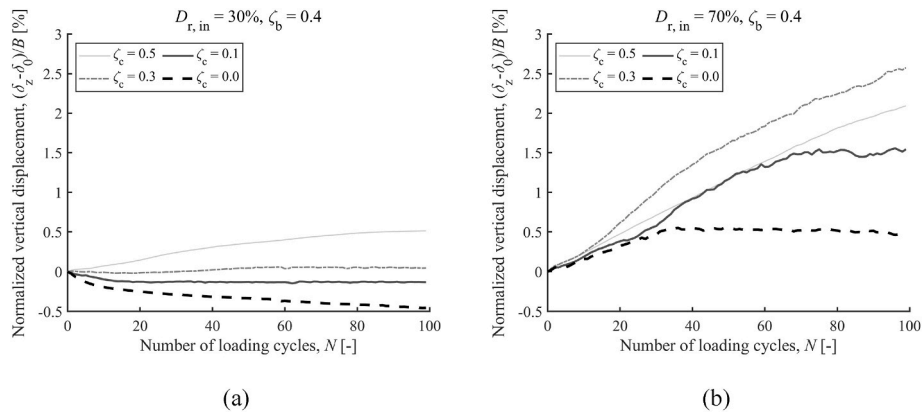
(a)

(b)

Fig. 18. Vertical displacement at the loading point varies with the number of loading cycles for different ζ_c under a constant $\zeta_b = 0.4$ (where δ_0 indicates the preloading displacement at the beginning of the first cycle). (a) In loose sand with $D_{r,in} = 30\%$, (b) in dense sand with $D_{r,in} = 70\%$.
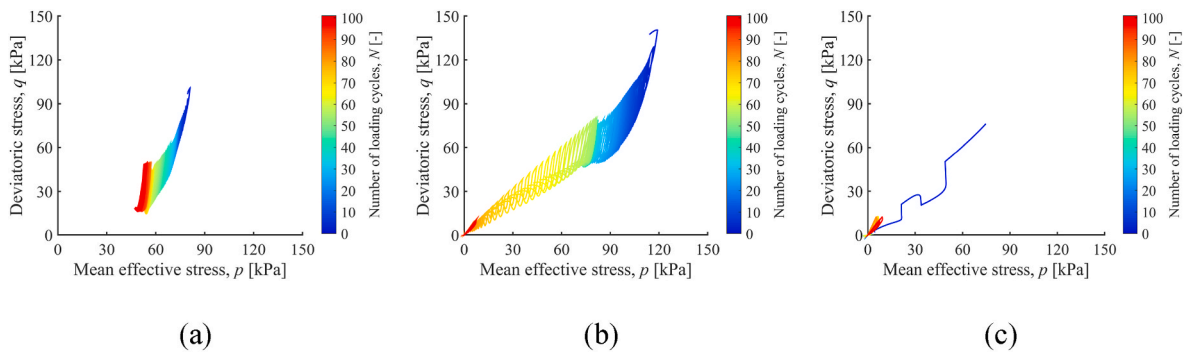

(a)

(b)

(c)

Fig. 19. Cyclic effective stress path of (a) element B, (b) element D, (c) element E, for case L2 with $D_{r,in} = 30\%$.
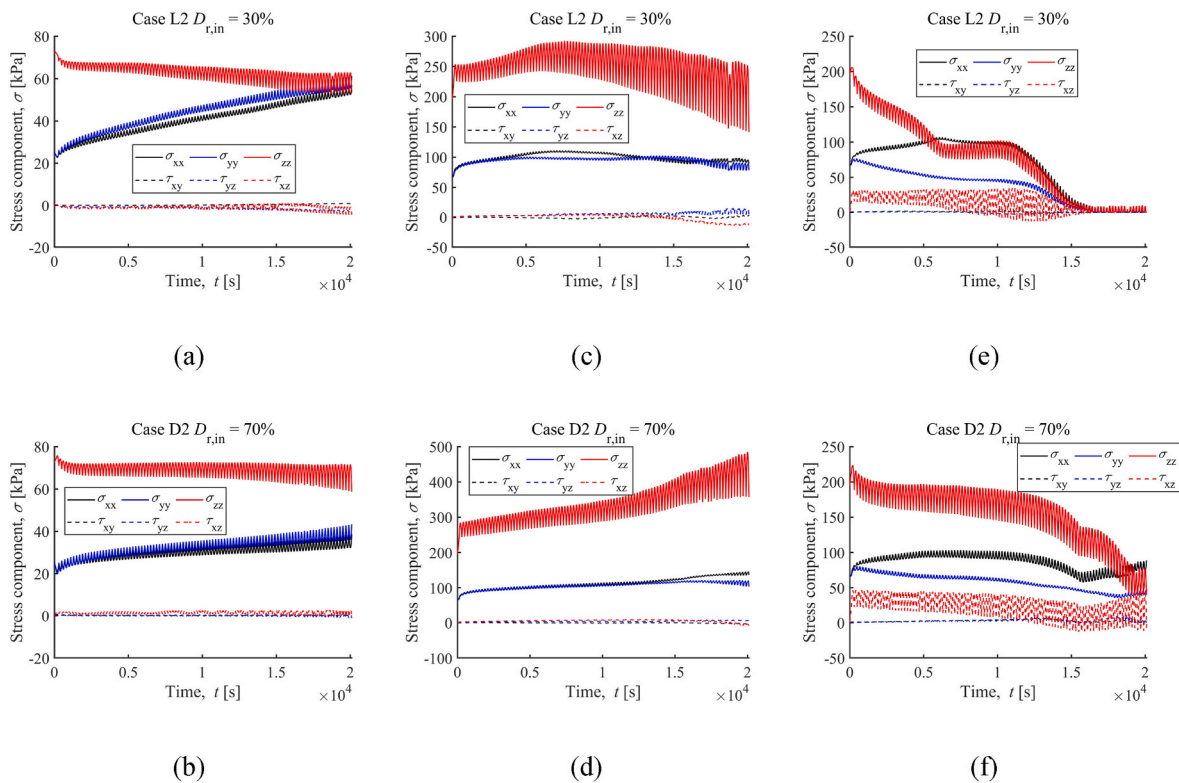

(a)

(c)

(e)

(b)

(d)

(f)

Fig. 20. Responses of element stress components for the reference elements in Fig. 1. (a)~(b) element A, (c)~(d) element C, (e)~(f) element D.

the preliminary study, the responses of elements B, D and E are comparable. As illustrated by the cyclic effective stress path (see Fig. 19) for case L2, both the mean effective stress and deviatoric stress decrease as the number of loading cycles increases for elements B, D and E. For the sake of simplicity, element D is used to represent the response of those three elements. Consequently, the responses of elements A, C, and D will be discussed and compared in the following sections.

The evolution of the six Cartesian stresses of the representative elements A, C and D during cyclic loading is demonstrated in Fig. 20. It can be observed that the three components of shear stress (τ_{xy}, τ_{yz}, τ_{xz}) of elements A and C remain nearly constant, with values close to zero. However, the component τ_{xz} of element D varies around an average value of 25 kPa and then decreases to values close to zero. The normal stress σ_{zz} for elements A gradually decreases in both loose and dense sand. In dense sand, σ_{zz} for element C increases progressively, whereas in loose sand, it initially increases and then decreases. During cyclic loading, the normal stress σ_{zz} of element D decreases and eventually reaches zero for loose sand and 50 kPa for dense sand.

Fig. 21 illustrates the cyclic effective stress paths of deviatoric stress versus mean effective stress, providing insight into the combination effect of the six stress components. The shaded sidebars in Fig. 21 represent the lode angle, ranging from 0° to 60°, where 0° and 60° indicate triaxial compression and extension, respectively. The initial state corresponds to the beginning of the first cycle.

Element A (located shallowly and directly above the plate anchor) exhibits a clear trend with an increase in mean effective stress and a decrease in deviatoric stress. The increase in mean effective stress is approximately twice as much in loose sand compared to dense sand. For element C (located deeply and directly above the plate anchor), the mean effective stress and deviatoric stress increase simultaneously in dense sand. In loose sand, there is an initial increase followed by a subsequent decrease. The stress path of element D (located deeply and on the right side above the plate anchor) differs from that of elements A and C. For element D, both the mean effective stress and deviatoric stress show a decreasing trend as the number of loading cycles increases,

eventually reaching zero in loose sand.

In Fig. 21(a)~(d), it is evident that the lode angle almost remains close to 0° throughout cyclic loading for elements A and C. This suggests that the soil directly above the plate anchor experiences a state similar to triaxial compression, or oedometer conditions. Therefore, a cyclic oedometer test would be suitable for evaluating the strength and stiffness of the soil in this region. On the other hand, the lode angle of element D varies between 0° and 60° during cyclic loading. This indicates the mobilization of the shear stress component, corresponding to the variations in τ_{xz} in Fig. 20(e)~(f). In this case, the DSS test would be more appropriate for measuring the strength and stiffness of the soil on the side above the plate anchor.

In Fig. 22, the stress path in $\tau_{xz}/p \sim (\sigma_{xx} - \sigma_{zz})/p$ plane is presented to further investigate the mobilized shear stress at element D. Initially, the stress state of element D lies on the negative side of the $(\sigma_{xx} - \sigma_{zz})/p$ axis, indicating that the horizontal stress is smaller than the vertical stress. As the number of loading cycles increases, the stress path gradually shifts towards the positive side of the $(\sigma_{xx} - \sigma_{zz})/p$ axis. After approximately 30 cycles of cyclic loading, the horizontal stress becomes higher than the vertical at loose sand; As a result, the shear stress τ_{xz} moves to the positive side of the $(\sigma_{xx} - \sigma_{zz})/p$ axis. This stress path implies that the principal stress axes for element D undergo rotation under cyclic loading, with the rotation being more pronounced in loose sand.

Fig. 23 shows the distribution of shear stress τ_{yz} and τ_{xz} in the overall soil domain at the end of the 100th cycle for case L2. The dash line indicates the mobilized zone of shear stress, which is located on the sides above and below the plate anchor. In these zones, the shear stress component cannot be neglected, and the soil's strength and stiffness can rely on the results of triaxial and DSS tests. To actually assess the soil's behaviour in these zones, it is necessary to measure and control more than three stress components simultaneously. Advanced test methods, such as hollow-cylinder torsional apparatus (HCTA) tests, can be employed to meet these requirements (Cheng et al., 2021; Liu and Kaynia, 2021).

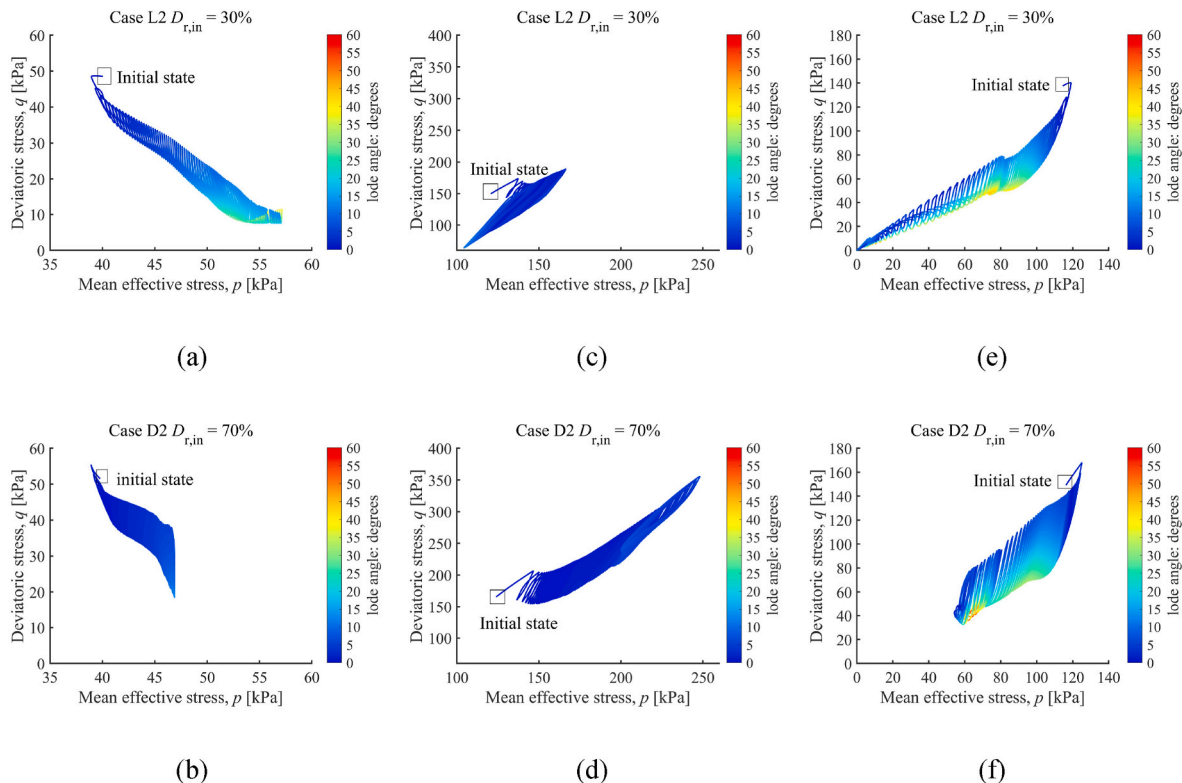Fig. 24 illustrates the cyclic strain responses for reference elements

Fig. 21. Cyclic effective stress path for the reference elements in Fig. 1. (a)~(b) element A, (c)~(d) element C, (e)~(f) element D.
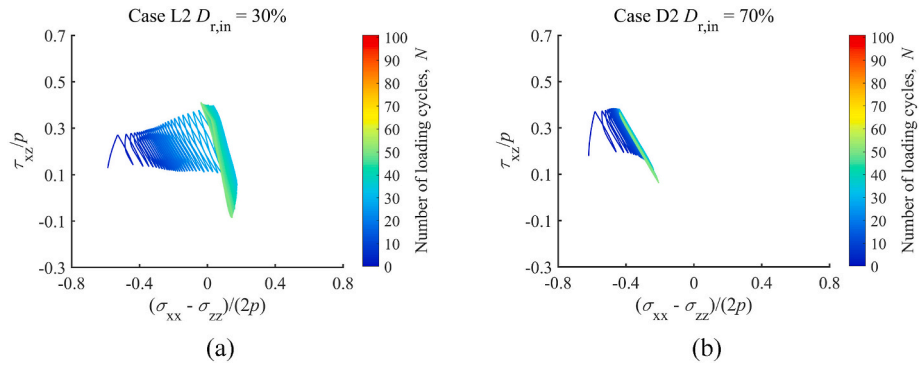
Fig. 22. Cyclic stress path in $\tau_{xz}/p \sim (\sigma_{xx} - \sigma_{zz})/(2p)$ plane for element D shown in Fig. 1. (a) Case L2 with initial relative density $D_{r,in} = 30\%$, (b) case D2 with initial relative density $D_{r,in} = 70\%$.

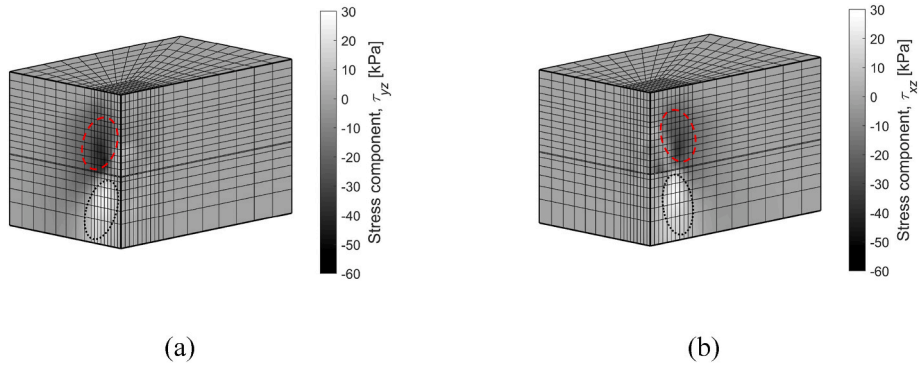**Fig. 23.** A sketch of shearing domain at the end of 100th cycles for case L2. (a) Stress component τ_{yz}, (b) stress component τ_{xz}.
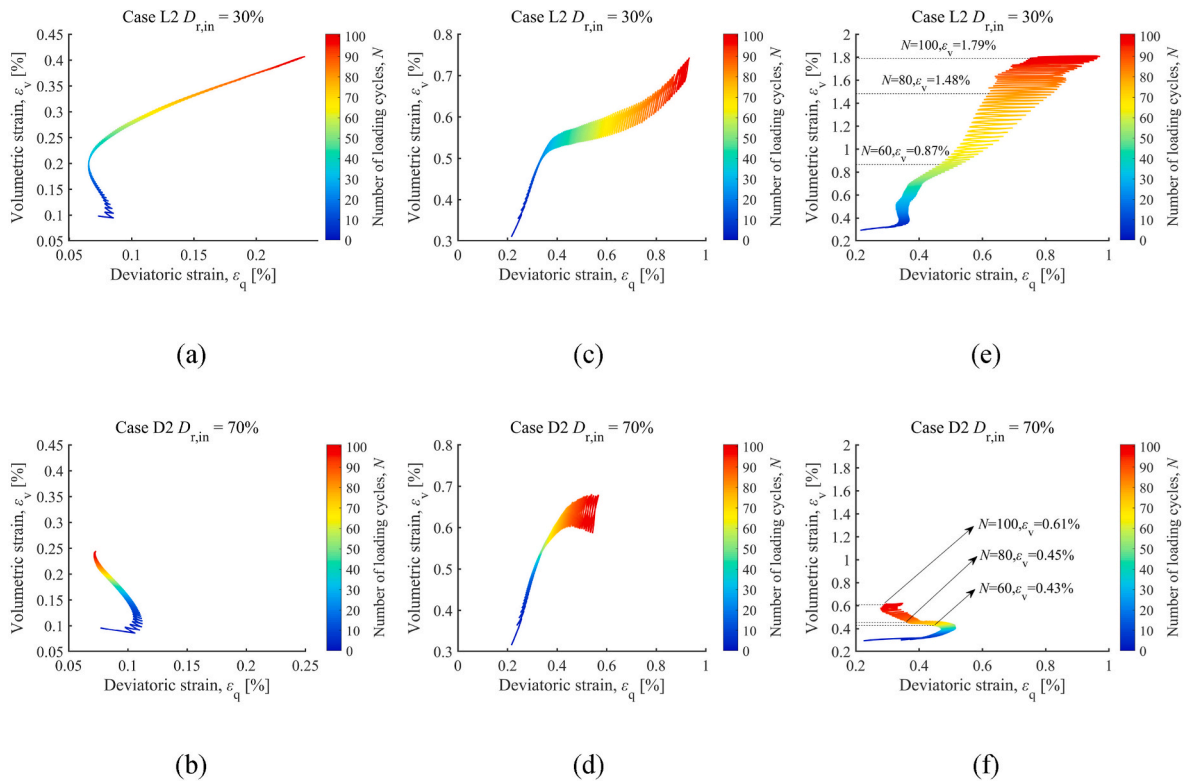

Fig. 24. Cyclic strain paths for the reference elements in Fig. 1. (a) Element A, (b) element C, (c) element D.

A, C, and D in both loose and dense sand, with the color bar indicating the number of loading cycles. The results highlight that the intensity of strain mobilized in the soil domain is greatly affected by the initial relative density of the soil and the location of the elements. Comparing Fig. 24 (a) and (c) or (b) and (d), it can be observed that the volumetric and deviatoric strains of element C are larger than those of element A for a given number of loading cycles. Furthermore, the rate of strain increase is higher in loose sand compared to dense sand, as evident from Fig. 24(a) and (b), (c) and (d), or (e) and (f). The findings indicate that there is substantial accumulation of volumetric and deviatoric strain in the early cyclic stage. For instance, as shown in Fig. 24(d), approximately 50% of the total strain accumulation is achieved in only about 30 cycles. This local response is consistent with the global response of the anchor, which experiences significant displacement accumulation in the early cyclic stage. Additionally, the soil in dense sand tends to reach a stable state more easily compared to loose sand.

4. Conclusion

This study systematically investigated the response of horizontally oriented rectangular plate anchors subjected to vertical monotonic and cyclic loads in a dry quartz sand. 3D FE simulations using the OpenSees platform were conducted, incorporating the upgraded SANISAND-MS constitutive model to capture the sand's cyclic behaviour. The soil-anchor interface below the plate anchor was modelled using the zeroLengthContact3D element, which allows for a gap to occur when the normal contact stress reaches zero. The discussion in this work covered the monotonic, cyclic, and post-cyclic behaviour of plate anchors, along with the local soil responses, to investigate the anchor-soil interaction mechanism. The intention was not to provide quantitative-level predictions.

Parametric studies were performed to investigate the influence of various factors on the plate anchor's behaviour, including the relative density, soil-anchor interface, embedded depth ratio, aspect ratio, cyclic amplitude ratio, and cyclic asymmetric ratio. The numerical result shows that when the soil-anchor interface does not allow for a gap, the uplift load is larger compared to the case where a gap is allowed, as the soil below the plate anchor contributes to shear resistance.

The findings regarding embedded depth ratio and aspect ratio were qualitatively consistent with experimental trends reported in the literature. The simulation results successfully captured the overshooting effect observed in the plate anchor's load-displacement response during the post-cyclic stage. This effect can be attributed to soil densification, which increases strength and stiffness, and creases a more stable sand micro-level configuration (fabric). Both factors result in a higher uplift load after cyclic loading compared to applying monotonic loading only. The degree of soil densification was found to be larger in loose sand compared to dense sand.

In summary, the result of this work helps to more deeply understand the mechanism of soil-anchor interaction, both from the global plate anchor perspective and the local soil response perspective. Further investigations could consider more general loading conditions, such as more anchor types and loading types, to further expand the knowledge in this field.

CRediT authorship contribution statement

Hongjian Lan: Methodology, Data Curation, Formal analysis, Software, Writing - Original Draft, Visualization. **Hongfen Zhao**: Conceptualization, Methodology, Validation, Writing - Review & Editing, Supervision, Funding acquisition. **Haoyuan Liu**: Conceptualization, Validation, Methodology, Writing - Review & Editing, Supervision, Software.

Declaration of competing interest

The authors declare that they have no known competing financial interests or personal relationships that could have appeared to influence the work reported in this paper.

Data availability

The authors do not have permission to share data.

Acknowledgements

Notation

A_0	'intrinsic' dilatancy parameter
B	plate anchor's breadth
c	compression-to-extension strength ratio
c_z	cohesion for *zeroLengthContact3D* element
c_h	hardening parameter
C_u	uniformity coefficient
D_{50}	median particle diameter
D_r	relative density
$D_{r,in}$	initial relative density
e_0	reference critical void ratio
e_{in}	initial void ratio
e_{max}	maximum void ratio
e_{min}	minimum void ratio
E_{steel}	Young's modulus of the elastic steel anchor
f	yield function
f_b	bounding function
f_m	memory function
F_{max}	maximum vertical load in a load cycle
F_{min}	minimum vertical load in a load cycle
F_{ref}	reference vertical load
h_0	hardening parameter

H	plate anchor's embedded depth
k	dimensionless bulk modulus
K_t	penalty in tangential direction for *zeroLengthContact3D* element
K_n	penalty in normal direction for *zeroLengthContact3D* element
L	plate anchor's length
m	Yield locus opening
M	Critical stress ratio in compression
n	nonlinearity parameter
N	number of loading cycles
n_b	void ratio dependence parameters
n_d	void ratio dependence parameters
p	mean effective stress
q	deviatoric stress
q^{ampl}	cyclic amplitude
Q	uplift load
$Q_{L/B=1.7}$	uplift load when $L/B = 1.7$
$\mathbf{S}$	deviatoric stress tensor
t	plate anchor's thickness
u_z	vertical displacement of soil domain
y	inherent anisotropy parameter
β	dilatancy memory parameter
δ_z	vertical displacement of the plate anchor
ε_q	deviatoric strain
ε_v	volumetric strain
ε_{acc}	accumulated total strain
η^{ave}	average shear stress ratio
ΔD_r	relative increment of relative density
ψ	state parameter
ρ	density for elastic steel anchor
ν	Poisson's ratio
ν_{steel}	Poisson's ratio for elastic steel anchor
γ	dry unit weight
λ_c	CSL shape parameters
μ_z	friction coefficient for *zeroLengthContact3D* element
μ_0	ratcheting parameter
ζ	memory surface shrinkage parameter
ζ_b	cyclic amplitude ratio
ζ_c	cyclic asymmetric ratio
ξ	CSL shape parameter
σ_{xx}	normal stress applied in x-direction
σ_{yy}	normal stress applied in y-direction
σ_{zz}	normal stress applied in z-direction
τ_{xy}	shear stress applied perpendicular to x-direction, along y-direction
τ_{xz}	shear stress applied perpendicular to x-direction, along z-direction
τ_{yz}	shear stress applied perpendicular to y-direction, along z-direction

References

Al Hakeem, N., Aubeny, C., 2019. Numerical investigation of uplift behaviour of circular plate anchors in uniform sand. J. Geotech. Geoenviron. Eng. 145, 04019039 https://doi.org/10.1061/(ASCE)GT.1943-5606.0002083.

Boushehrian, A.H., Hataf, N., Ghahramani, A., 2009. Numerical study of cyclic behaviour of shallow foundations on sand reinforced with geogrid and grid-anchor. Int. J. Civ. Environ. Eng. 3, 390–393.

Balomenos, G.P., Kameshwar, S., Padgett, J.E., 2020. Parameterized fragility models for multi-bridge classes subjected to hurricane loads. Eng. Struct. 208, 110213 https://doi.org/10.1016/j.engstruct.2020.110213.

Corti, R., Diambra, A., Wood, D.M., Escribano, D.E., Nash, D.F., 2016. Memory surface hardening model for granular soils under repeated loading conditions. J. Eng. Mech. 142 (12), 04016102.

Cassidy, M.J., Gaudin, C., Randolph, M.F., Wong, P.C., Wang, D., Tian, Y., 2012. A plasticity model to assess the keying of plate anchors. Geotechnique 62 (9), 825–836.

Cheng, Xiaoyang, Diambra, A., Ibraim, E., Liu, H., Pisanò, F., 2021. 3D FE-informed laboratory soil testing for the design of offshore wind turbine monopiles. JMSE 9, 101. https://doi.org/10.3390/jmse9010101.

Choudhary, A.K., Pandit, B., Babu, G.L.S., 2018. Three-dimensional analysis of uplift behaviour of square horizontal anchor plate in frictional soil. Int. J. Geosynth. Ground Eng. 4, 14. https://doi.org/10.1007/s40891-018-0130-1.

Chow, S.H., O'Loughlin, C.D., Corti, R., Gaudin, C., Diambra, A., 2015. Drained cyclic capacity of plate anchors in dense sand: experimental and theoretical observations. Géotech. Lett. 5, 80–85. https://doi.org/10.1680/geolett.15.00019.

Chow, S.H., O'Loughlin, C.D., Gaudin, C., Lieng, J.T., 2018. Drained monotonic and cyclic capacity of a dynamically installed plate anchor in sand. Ocean Eng. 148, 588–601. https://doi.org/10.1016/j.oceaneng.2017.11.051.

Chow, S.H., Diambra, A., O'Loughlin, C.D., Gaudin, C., Randolph, M.F., 2020. Consolidation effects on monotonic and cyclic capacity of plate anchors in sand. Geotechnique 70 (8), 720–731. https://doi.org/10.1680/jgeot.19.TI.017.

Dafalias, Y.F., Papadimitriou, A.G., Li, X.S., 2004. Sand plasticity model accounting for inherent fabric anisotropy. J. Eng. Mech. 130, 1319–1333. https://doi.org/10.1061/(ASCE)0733-9399(2004)130:11(1319).

Dickin, E.A., Laman, M., 2007. Uplift response of strip anchors in cohesionless soil. Adv. Eng. Software 38, 618–625. https://doi.org/10.1016/j.advengsoft.2006.08.041.

Evans, T.M., 2019. Three-dimensional simulations of plate anchor pullout in granular materials. Int. J. GeoMech. 14.

Fontana, C.M., Arwade, S.R., DeGroot, D.J., Myers, A.T., Landon, M., Aubeny, C., 2016. Efficient multiline anchor systems for floating offshore wind turbines. In: ASME 2016 35th International Conference on Ocean, Offshore and Arctic Engineering, vol. 6. American Society of Mechanical Engineers (ASME), New York, NY, USA. https://doi.org/10.1115/OMAE2016-54476 ocean space utilization; ocean renewable energy.

Ghaly, A.M., 1997. Load-displacement prediction for horizontally loaded vertical plates. J. Geotech. Geoenviron. Eng. 123, 74–76.

Hanna, A., Ayadat, T., Sabry, M., 2007. Pullout resistance of single vertical shallow helical and plate anchors in sand. Geotech. Geol. Eng. 25, 559–573.

Houlsby, G.T., Abadie, C.N., Beuckelaers, W.J.A.P., Byrne, B.W., 2017. A model for nonlinear hysteretic and ratcheting behaviour. Int. J. Solid Struct. 120, 67–80. https://doi.org/10.1016/j.ijsolstr.2017.04.031.

Hallowell, S.T., Arwade, S.R., Fontana, C.M., DeGroot, D.J., Aubeny, C., Diaz, B.D., Myers, A.T., Landon, M., 2018. System reliability of floating offshore wind farms with multiline anchors. Ocean. Eng. 160, 94–104.

Houlsby, G.T., Amorosi, A., Rollo, F., 2019. Non-linear anisotropic hyperelasticity for granular materials. Comput. Geotech. 115, 103167 https://doi.org/10.1016/j.compgeo.2019.103167.

Huang, R., Zhang, M., Guo, M., Ye, R., Fu, C., Shen, D., 2020. Study on mooring economy and stability of floating wind turbine. In: 2020 5th Asia Conference on Power and Electrical Engineering (ACPEE). Presented at the 2020 5th Asia Conference on Power and Electrical Engineering (ACPEE). IEEE, Chengdu, China, pp. 308–312. https://doi.org/10.1109/ACPEE48638.2020.9136319.

Lan, H., Liu, H.Y., Zhao, H., 2023. Impact of hyper-elasticity on cyclic sand modelling: a numerical study based on SANISAND-MS. Comput. Geotech. 159, 105428 https://doi.org/10.1016/j.compgeo.2023.105428.

LeBlanc, C., Houlsby, G., Byrne, B., 2010. Response of stiff piles in sand to long-term cyclic lateral loading. Geotechnique 60, 79–90.

Li, Z., Liu, H., Zhao, Y., 2016. Large Deformation Numerical Analysis of the Ultimate Pullout Capacity of Plate Anchors in Sand.

Liang, W., Zhao, J., Wu, H., Soga, K., 2021. Multiscale modeling of anchor pullout in sand. J. Geotech. Geoenviron. Eng. 147, 04021091.

Liu, H.Y., Diambra, A., Abell, J.A., Pisanò, F., 2020. Memory-Enhanced plasticity modeling of sand behaviour under undrained cyclic loading. J. Geotech. Geoenviron. Eng. 146, 04020122 https://doi.org/10.1061/(ASCE)GT.1943-5606.0002362.

Liu, H.Y., Kaynia, A.M., 2021. Characteristics of cyclic undrained model SANISAND-MSu and their effects on response of monopiles for offshore wind structures. Geotechnique 1–16. https://doi.org/10.1680/jgeot.21.00068.

Liu, H.Y., Kementzetzidis, E., Abell, J.A., Pisanò, F., 2022a. From cyclic sand ratcheting to tilt accumulation of offshore monopiles: 3D FE modelling using SANISAND-MS. Geotechnique 72, 753–768. https://doi.org/10.1680/jgeot.20.P.029.

Liu, H.Y., Pisanò, F., Jostad, H.P., Sivasithamparam, N., 2022b. Impact of cyclic strain accumulation on the tilting behaviour of monopiles in sand: an assessment of the Miner's rule based on SANISAND-MS 3D FE modelling. Ocean Eng. 250, 110579 https://doi.org/10.1016/j.oceaneng.2022.110579.

Liu, H.Y., Abell, J.A., Diambra, A., Pisanò, F., 2019. Modelling the cyclic ratcheting of sands through memory-enhanced bounding surface plasticity. Geotechnique 69, 783–800. https://doi.org/10.1680/jgeot.17.P.307.

McGann, C.R., Arduino, P., Mackenzie-Helnwein, P., 2015. A stabilized single-point finite element formulation for three-dimensional dynamic analysis of saturated soils. Comput. Geotech. 66, 126–141.

McKenna, F., 2011. OpenSees: a framework for earthquake engineering simulation. Comput. Sci. Eng. 13, 58–66.

Merifield, R.S., Lyamin, A.V., Sloan, S.W., 2006. Three-dimensional lower-bound solutions for the stability of plate anchors in sand. Geotechnique 56, 123–132. https://doi.org/10.1680/geot.2006.56.2.123.

Merifield, R.S., Sloan, S.W., 2006. The Ultimate Pullout Capacity of Anchors in Frictional Soils, vol. 43, p. 17.

Moghaddas Tafreshi, S.N., Rahimi, M., Dawson, A.R., Leshchinsky, B., 2019. Cyclic and post-cycling anchor response in geocell-reinforced sand. Can. Geotech. J. 56, 1700–1718. https://doi.org/10.1139/cgj-2018-0559.

O'Loughlin, C.D., Barron, B., 2012. Capacity and keying response of plate anchors in sand. In: Offshore Site Investigation and Geotechnics: Integrated Technologies-Present and Future. Society of Underwater Technology.

Peccin da Silva, A., Diambra, A., Karamitros, D., Chow, S.H., 2021. A non-associative macroelement model for vertical plate anchors in clay. Can. Geotech. J. 58 (11), 1703–1715.

Peccin da Silva, A., 2021. Macro-element Modelling of Plate Anchors for Floating Offshore Structures Accounting for Capacity Changes during Operational Conditions. Doctoral dissertation, University of Bristol.

Rowe, R.K., Davis, E.H., 1982. The behaviour of anchor plates in sand. Geotechnique 32, 25–41. https://doi.org/10.1680/geot.1982.32.1.25.

Rigzone, 2006. Permanent SEPLA mooring unit installed in Gulf. Rigzone Mag. www.rigzone.com/news/article.asp?a_id=30962S. (Accessed 4 April 2006).

Roy, A., Chow, S.H., O'Loughlin, C.D., Randolph, M.F., 2021. Towards a simple and reliable method for calculating uplift capacity of plate anchors in sand. Can. Geotech. J. 58, 1314–1333. https://doi.org/10.1139/cgj-2020-0280.

Roy, Anamitra, O'Loughlin, C.D., Chow, S.H., Randolph, M.F., 2021. Inclined loading of horizontal plate anchors in sand. Geotechnique 17.

Schofield, A.N., Wroth, P., 1968. Critical State Soil Mechanics. McGraw-hill, London.

Tsuha, C.H.C., Foray, P.Y., Jardine, R.J., Yang, Z.X., Silva, M., Rimoy, S., 2012. Behaviour of displacement piles in sand under cyclic axial loading. Soils Found. 52, 393–410. https://doi.org/10.1016/j.sandf.2012.05.002.

Vesić, A.S., 1973. Analysis of ultimate loads of shallow foundations. J. Soil Mech. Found Div. 99, 45–73.

Vorpahl, F., Schwarze, H., Fischer, T., Seidel, M., Jonkman, J., 2013. Offshore wind turbine environment, loads, simulation, and design: OWT loads and design. WENE 2, 548–570. https://doi.org/10.1002/wene.52.

White, D.J., Cheuk, C.Y., Bolton, M.D., 2008. The uplift resistance of pipes and plate anchors buried in sand. Geotechnique 58, 771–779. https://doi.org/10.1680/geot.2008.3692.

Wichtmann, T., Niemunis, A., Triantafyllidis, Th, 2005. Strain accumulation in sand due to cyclic loading: drained triaxial tests. Soil Dynam. Earthq. Eng. 25, 967–979. https://doi.org/10.1016/j.soildyn.2005.02.022.

Yang, M., Aubeny, C.P., Murff, J.D., 2012. Behavior of suction embedded plate anchors during keying process. J. Geotech. Geoenviron. Eng. 138 (2), 174–183.

Yao, Y.P., Hou, W., Zhou, A.N., 2009. UH model: three-dimensional unified hardening model for overconsolidated clays. Geotechnique 59 (5), 451–469.

Yao, Y.P., Liu, L., Luo, T., Tian, Y., Zhang, J.M., 2019. Unified hardening (UH) model for clays and sands. Comput. Geotech. 110, 326–343.

Zhang, N., Wu, H.-N., Shen, J.S.-L., Hino, T., Yin, Z.-Y., 2017. Evaluation of the uplift behaviour of plate anchor in structured marine clay. Mar. Georesour. Geotechnol. 35, 758–768. https://doi.org/10.1080/1064119X.2016.1240273.